



# Automatic detection of field line resonance frequencies in the Earth's plasmasphere

Raffaello Foldes<sup>1,2</sup> · Alfredo Del Corpo<sup>3</sup> · Gianluca Napoletano<sup>1</sup> · Ermanno Pietropaolo<sup>1</sup> · Massimo Vellante<sup>1</sup>

Received: 1 May 2023 / Accepted: 10 September 2023 / Published online: 3 October 2023  
© The Author(s), under exclusive licence to Accademia Nazionale dei Lincei 2023

## Abstract

Ground-based magnetometer stations represent a multi-viewpoint and easy-to-access system for sounding Earth's magnetic field disturbances in the inner magnetosphere. Using Ultra-Low Frequency (ULF) measurements recorded from pairs of meridionally aligned stations, it is possible to determine the Field Line Resonance (FLR) frequencies, which are directly related to the equatorial magnetospheric plasma mass density. Recently, it has been shown by Foldes et al. (J Geophys Res 126(5):e2020JA029008. <https://doi.org/10.1029/2020JA029008>, 2021) that the Machine Learning (ML) algorithms are valuable tools for detecting FLRs by exploiting the useful information provided by cross-phase Fourier spectra, which are at the heart of the ULF technique for inferring the magnetospheric mass density. The main shortcoming of this approach is that it is not possible to discriminate between active and quiet times in terms of resonances. It is commonly known that detecting FLRs using cross-phase spectra may often be unfeasible due to data gaps, noisy signals, and/or quiescent ULF wave periods. To handle these situations, we implement an ML classification algorithm to identify periods when the resonance frequencies are observable and thus easily estimated. Our algorithm can distinguish samples into three main classes: periods with observed frequency ("Freq" class) from others ("NoFreq"), and, in addition, it can determine whether the considered field line crosses the plasmasphere boundary layer (PBL or plasmopause) at a given time. The results of our method are validated for a particular pair of stations (at  $L = 2.9$ ) along the Equatorial quasi-Meridional Magnetometer Array (EMMA), using a large dataset comprising different geomagnetic conditions. The proposed approach might be combined with a regression algorithm (such as those proposed in Foldes et al. (J Geophys Res 126(5):e2020JA029008. <https://doi.org/10.1029/2020JA029008>, 2021)) in a two-stage ML pipeline, with the ultimate goal of implementing a completely automated system for the real-time monitoring of the plasmasphere dynamics from ground-based magnetometer stations.

**Keywords** Geomagnetic field line resonance · Plasmaspheric mass density · Inner magnetosphere · Machine learning · Space weather

Alfredo Del Corpo, Gianluca Napoletano, Ermanno Pietropaolo, and Massimo Vellante have contributed equally to this work.

This paper belongs to the Topical collection "Frontiers in Italian studies on Space Weather and Space Climate", that includes papers written on the occasion of the Second National Congress of SWICo, "Space Weather Italian Community", held on February 9-11 2022 in Rome at ASI, "Agenzia Spaziale Italiana".

✉ Raffaello Foldes  
raffaello.foldes@ec-lyon.fr

- <sup>1</sup> Department of Physical and Chemical Sciences, University of L'Aquila, L'Aquila, Italy
- <sup>2</sup> Univ Lyon, CNRS, École Centrale de Lyon, INSA Lyon, Univ Claude Bernard Lyon I, LMFA UMR 5509, 69134 Ecully cedex, France
- <sup>3</sup> Istituto Nazionale di Geofisica e Vulcanologia, INGV, Viale Crispi 43, 67100 L'Aquila, Italy

## 1 Introduction

The Earth's plasmasphere is a crucial region for Space Weather because of its dominant contribution to the mass content of the inner magnetosphere, and then in determining the magnetohydrodynamic response of the magnetosphere to solar wind perturbations. The plasmasphere is mainly composed of low energy plasma (at  $\sim 1eV$ ) of ionospheric origin. It can extend up to approximately  $6R_E$ , even though its shape and extension significantly vary between day and night and with different geomagnetic conditions (Sandel et al. 2003). This region has seen a surge of interest in recent years for its importance in wave-particle interactions (Thorne 2010; Liemohn 2006) and because of its coupling with the underlying layer, the ionosphere (Chappell 2015);

in addition, the outer boundary, called the plasmopause [or plasmasphere boundary layer, PBL (Carpenter and Lemaire 2004)] represents a direct information source for the strength of the solar wind and solar storms impact as, for instance, it may move earthward up to 1.5–2  $R_E$  during major geomagnetic storms (Obana et al. 2019). The plasma, trapped in an approximately dipolar magnetic field configuration, also varies in composition (Roberts et al. 1987; Del Corpo et al. 2022) and density (Carpenter and Anderson 1992; Ozhogin et al. 2012), with this latter ranging over several orders of magnitude and, in particular, decreasing when moving away from the Earth. The PBL also marks the region where the plasma density drastically drops (Liu et al. 2015; Cho et al. 2015). In the last decades, mostly empirical, but also theoretical and hybrid models have been developed to predict the position and dynamics of the plasmopause (see, e.g., Cho et al. (2015); Carpenter and Anderson (1992); O'Brien and Moldwin (2003); Ripoll et al. (2023); Goldstein et al. (2019); Pierrard and Voiculescu (2011); Del Corpo et al. (2020)). In a simple dipolar approximation of the magnetic field lines, it has been shown that the equatorial plasma density at a distance  $L$  from Earth, where  $L$  is the McIlwain parameter, can be inferred from the measure of the resonance frequency  $\rho_L \sim 1/f_L^2$  of the field line crossing the equator at  $L$  (Cummings et al. (1969)). This can be obtained by considering the magnetic field lines as vibrating strings with two fixed ends, which is a suitable approximation when the ionospheric conductivity is very high (i.e., infinite conductivity approximation), and therefore especially when both the field line footprints are on the day side. The knowledge of the field line resonance (FLR) frequency, assuming a proper magnetic field model and mass density profile along the line (see Del Corpo et al. (2019) and reference therein), allows us to estimate the equatorial plasma density by solving the wave equation proposed by Singer et al. (1981). FLRs can be measured using ground-based magnetometer stations, such as those of the European quasi-Meridional Magnetometer Array (EMMA, see Lichtenberger et al. (2013)). They represent a reliable and longstanding multi-viewpoint of the plasmaspheric dynamics. The estimation of FLR frequencies from magnetometer measurements is obtained through a dynamical Fourier cross-spectral analysis of the signals of two stations separated in latitude around 1–3° and approximately aligned along a magnetic meridian. The method was proposed by Baransky et al. (1985) and then developed by Waters et al. (1991). It is mainly based on the assumption that resonance frequencies decrease along a meridian when moving poleward and vary linearly for small displacements.

Hence, the resonance frequency of a field line having one footprint at the mid-point between two stations is evaluated by computing the cross-phase ( $\Delta\varphi = \varphi_2 - \varphi_1$ ) and

the amplitude ratio  $A_2/A_1$  from the Fourier spectra of the North–South component of the measured signal; here, the first station ( $S_1$ ) is considered to be poleward. In these conditions, FLR frequencies are identified as frequencies where the cross-phase peaks and, simultaneously, the amplitude ratio crosses unity with a positive slope. However, the radial behavior of the FLR frequency inverts across a steep plasmopause, and a cross-phase minimum (rather than a maximum) may be detected if the two stations map near the plasmopause (Menk et al. 2004; Kale et al. 2007). The situation can be re-established by reversing the order of the two stations when computing the cross-spectrum (Del Corpo et al. 2019) (e.g.,  $\Delta\varphi_{PBL} = -\Delta\varphi = \varphi_1 - \varphi_2$ ). The first attempt to estimate FLRs by exploiting the information given by the Fourier cross-phase analysis in combination with Machine Learning (ML) techniques was made by Foldes et al. (2021) (hereafter F21). In that work, the authors adopted several ML algorithms for estimating resonance frequencies using the EMMA measurements, at various latitudes and different geomagnetic conditions. The results showed good agreement between the validated and estimated frequencies. Nevertheless, the main limitation of this approach, in view of its use for real-time (or near real-time) monitoring of the plasmasphere, is that it works only with samples where resonances are effectively triggered, producing a clear evidence in the cross-phase spectra. This is not generally true; apart from quiescent ultra-low frequency periods (Balasis et al. 2019), detecting FLR frequencies may be problematic for a low signal-to-noise ratio and instrumental issues, such as data gaps. Therefore, to implement a completely automated procedure based on ML algorithms, we propose a classification algorithm for discriminating samples with an observed resonance from the others. The method adopts a tree-based classification algorithm, named eXtreme Gradient Boosting (XGB, Chen and Guestrin (2016)), to first perform a binary classification into frequency (“Freq”) and no frequency (“NoFreq”) samples, then pointing to a more challenging multi-class approach. In this latter, samples with resonance frequencies observed in correspondence to a minimum of the cross-phase are classified separately in a third class, namely “PBL”. By combining this approach with the one proposed in Foldes et al. (2021), it is possible to develop an automated monitoring procedure, to efficiently analyze long-time intervals, and to produce extensive statistics useful for further study. The present manuscript is organized by describing the data set used in the analysis in Sect. 2. Section 3 widely explains the ML procedures, including data pre-processing and transformation. The results are shown in Sect. 4, first for the binary and then for multi-classification approaches. Finally, in Sect. 5, the novel introduced algorithm is applied in combination with the one proposed in Foldes et al. (2021) on a test set including a geomagnetic storm.

## 2 Data

The data set adopted in this analysis extends the one already used in Foldes et al. (2021) for the pair of mid-latitude EMMA stations Tartu-Birzai (hereafter TAR-BRZ). In fact, in this case, we include also times when a resonance was not observed, so the data set consists of a more significant number of samples ( $N = 14,910$ ) covering several intervals between 2012 and 2018, as summarized in detail in Table 1. The data set comprises very different geomagnetic conditions, ranging from long-standing quiescent periods to moderate and strong geomagnetic storms that have been studied and characterized in several studies (Piersanti et al. 2017; Pezzopane et al. 2019; Vellante et al. 2021; Del Corpo and Vellante 2023). The data set consists of Fourier cross-phase spectra and, where available, validated fundamental resonance frequencies calculated every 30 min through a well-established procedure implemented by Del Corpo et al. (2019); this ensures reliable frequencies and cross-phase spectra with high resolution. The spectra are computed every 30 min over a 2-h running window. In addition, the resulting spectrum can be smoothed over a selectable range of frequencies (11 or more) to reduce the statistical fluctuations.

The data set includes daytime and nighttime frequencies, which are the subject of analysis in this work, although the reliability of nighttime resonance frequencies is still debated. Indeed, the night-side region of the Earth's magnetosphere, particularly the conductivity level of the underlying ionospheric layer (Allan and Knox 1979), may not be suitable for sustaining standing Alfvén waves. Consequently, the observed frequencies might correspond to free-end modes in these situations. Another particular condition occurs when one footprint of the resonant field line is in the dawn/dusk sector (hereafter “penumbra”); in this case, quarter-wave modes are likely to be observed (Obana et al. 2008, 2015). The various analyses performed in our ML framework try to consider all of these possible situations, either *a priori* to better evaluate the performance of our algorithms under different conditions, or *a posteriori* to have a clearer interpretation of the results.

The data set is divided on a time-basis into training (70%) and test set (30%). Notably, the training set spans

from DoY 266, 2012, to DoY 235, 2015; the remaining days are in the test set. This particular division is adopted to ensure, at first, that training and test sets are not correlated, as it might happen when they are randomly selected. Second, but most importantly, the percentage between the different classes is the same in the train and test sets (see Fig. 1); this makes these sets as representative as possible of the entire data set. The latter choice is important, in particular, when dealing with highly unbalanced data sets. In addition, a time-basis split resembles what will happen in an operational scenario, when the FLR frequencies are estimated on the new data, while the past information are available for training. Figure 1 shows in panel (a) the number of samples divided into three classes (i.e., “NoFreq”, “Freq” and “PBL”) and in panel (b) for the binary classification. Panels c) and d) in Fig 1 show the histograms of the indices  $Kp$  and  $Dst$  for the training and test set. The two indices, among many others, are commonly used to evaluate the intensity of geomagnetic disturbances. We can appreciate how the division of the data set represents the variety of geomagnetic conditions that can be observed in our data; this also ensures homogeneity between the training and test sets. The input data are available at <https://doi.org/10.5281/zenodo.8321186> (Foldes et al. 2023).

## 3 Methods

The input, composed of one-dimensional (1D) Fourier cross-phase spectra, is normalized (as in Foldes et al. (2021)) before applying the classification procedure. Data normalization is often applied, especially in the case of data composed of variables with extensive numerical ranges; this is done to improve the performance of ML algorithms, since they compute gradients in the back-propagation process, which are particularly sensitive to the magnitude of the input variables. Then, each sample is prepared by assigning a specific class: “NoFreq” if no resonance frequency has been observed, “Freq” if there is a validated frequency for that sample and “PBL” when the frequency has been presumably evaluated across the plasmasphere boundary layer. This classification is helpful, especially in recognizing the latter; indeed, as mentioned earlier, the cross-phase for estimating the FLR frequency

**Table 1** Detail of the data set of Tartu-Birzai: Lat. 57.2°, Lon. 25.6°, L=2.9

YEAR	2012	2013	2014	2015	2016	2017	2018
DoY	266–336	72–86 145–162 177–200 275–287	45–68	72–90 98–116 169–178 224–245 352–362	15–30 284–295	146–153 195–209 248–264	234–246
# samples	3,335	3,262	1,121	3,743	1,213	1,612	624

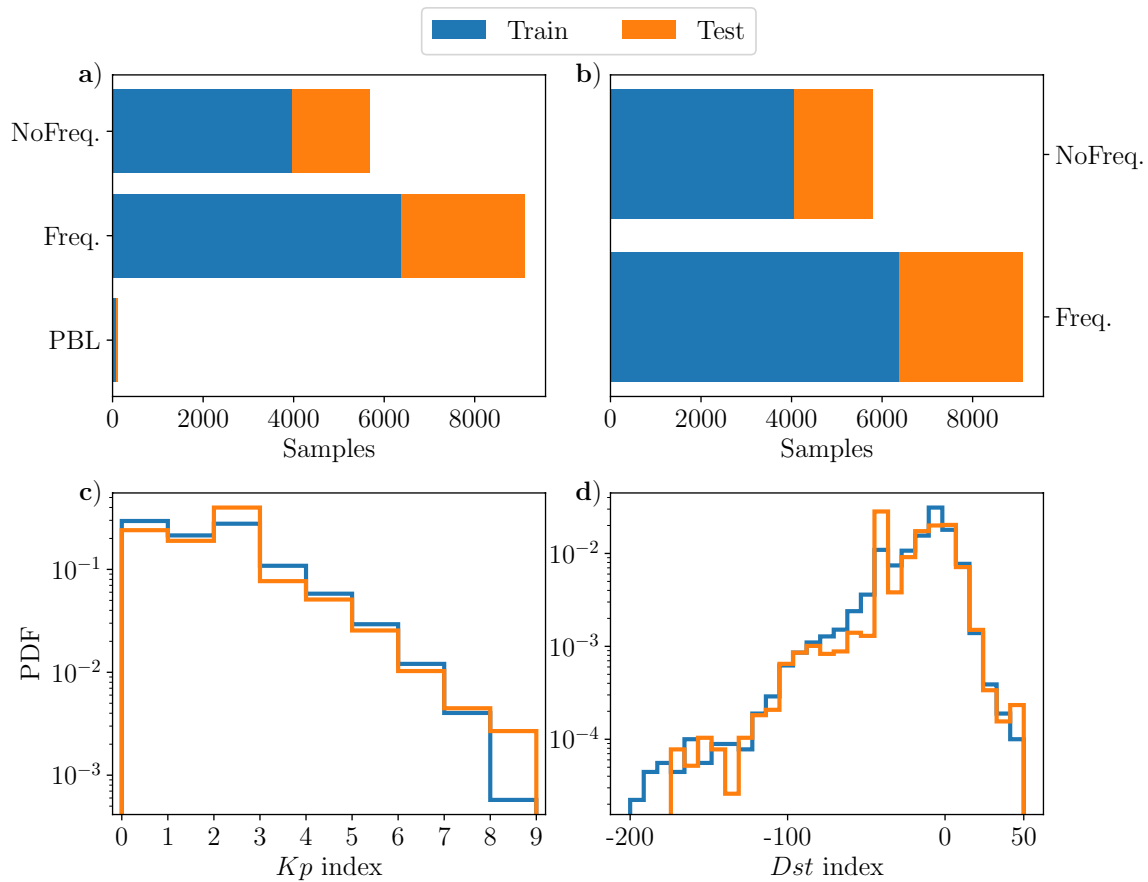


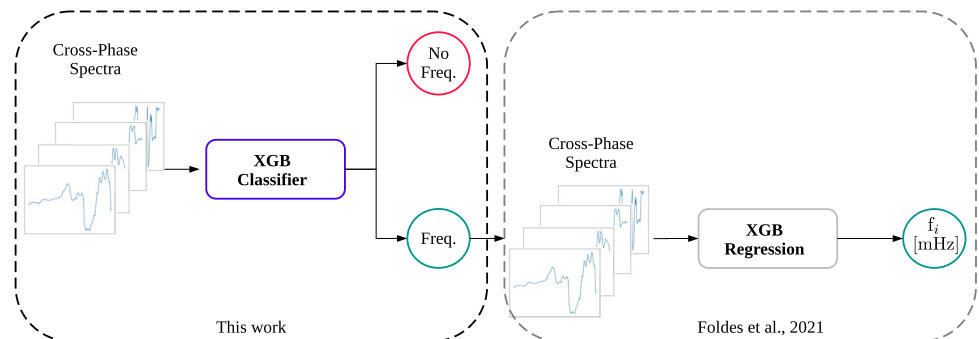
**Fig. 1** Overview of the data set divided into training (blue) and test (orange) set for the considered classes (i.e., “NoFreq”, “Freq” and “PBL”). Panels **a** and **b** show the histogram of the classes for both the binary, b), and multi-classification, **a** problem. The data set is divided

into 70% training and 30% test on a time-basis. Panels **c** and **d** show the Probability Distribution Function (PDF) of the *Kp* and *Dst* indices, respectively, for the training and test sets (color figure online)

needs to be reversed in this situation. In this analysis, we compare the multi-classification approach (i.e., 3 classes) with a binary classification for two main reasons: first, the inclusion of “PBL” samples is not important for every pair of stations, since the position of the plasmopause may reach low latitudes only during extremely severe

geomagnetic storms. Second, the plasmopause samples are generally a tiny percentage of the entire data set, also at higher latitudes, representing a challenging addition to the classification problem that has to be compared with the possible advantages achievable by considering them. In the case of binary classification, the samples initially defined as “PBL” are assigned to the “NoFreq” class.

**Fig. 2** Schematic representation of the automated procedure of the field line resonance frequencies detection with a binary classification as the first stage. If a multi-class classification is instead adopted, both “Freq” and “PBL” samples are moved to the regression stage



### 3.1 Classification algorithm

The classification algorithm represents the first step of the ML procedure (left block of Fig. 2), and it has been developed employing the XGB algorithm (Chen and Guestrin 2016). XGB is an efficient and versatile package for applying tree-based boosting algorithms, which provides high accuracy in various problems and good scalability with high-dimensional datasets. Recently, the XGB algorithm has been successfully used to tackle several regression and classification problems in ML; Foldes et al. (2021) showed that it represents the optimal choice among the tested algorithms in estimating FLR frequencies from cross-phase spectra at different latitudes and for variable geomagnetic conditions. The classification algorithm takes as input cross-phase spectra averaged over 2 h and sampled every 30 min (being the time resolution of the validated frequencies) and returns the probability vector  $\mathbf{p}$  whose components must verify  $\sum_i p_i = 1$ , with  $i$  ranging in the number of classes and indicating the probability that a given sample belongs to the  $i$ th class. The predicted class, for the  $j$ th sample, is then determined as the class with the maximum probability,  $c_j = \arg \max_i [p_{ij}]$ . After the classification stage, all the samples classified as "Freq" automatically move to the next step, which involves estimating the FLR frequency values. The technique, implemented in Foldes et al. (2021) (right block in Fig. 2), uses the XGB as the regression algorithm with the same cross-phase spectra as input. In the case of the multi-classification approach, even the "PBL" samples move to the regression step, but the input data must be modified before estimating the resonance frequency value. Indeed, as already introduced, the cross-phase technique for pairs of stations mapping across the plasmopause can be applied by inverting the order of signals before the Fourier cross-analysis; this can also be expressed in terms of reversing the cross-phase spectrum ( $\Delta\varphi_{PBL} = -\Delta\varphi$ ) computed with the usual order (i.e., poleward station as the first point). All the remaining samples, classified as "NoFreq", are discarded at this stage. However, the pipeline could be enriched by including additional steps that perform other tests on the excluded samples to minimize the loss of information further. The entire procedure is depicted in Fig. 2, and it is designed to be included in the ASI (Italian Space Agency) Space Weather Infrastructure [Caesar project (Laurenza et al. 2023)], which includes the plasma mass density sounding by EMMA measurements.

### 3.2 Moving threshold technique

In ML classification algorithms, the amount of samples per class is often crucial to creating a model that can generalize its performance to many real-world applications. Usually, working with imbalanced classes leads to an algorithm prone to overpredict the predominant class and to a higher

classification error rate for the other, which in many situations is the class of interest (see e.g., Stumpo et al. (2021)). As shown in Fig. 1, our data set manifests different levels of imbalance when considering a binary or a multi-classification problem. Indeed, in the case of only two classes (top-right panel), the ratio between "NoFreq" (NF) and "Freq" (F) samples is  $\approx 0.5$ , while for the multi-classification (top-left panel), the ratio between "PBL" samples and "Freq" is  $\approx 0.013$  and between "PBL" and "NoFreq"  $\approx 0.020$ . The probability threshold is generally set by default to 0.5 for binary classifications, which is often not the optimal choice for imbalanced data. Therefore, adjusting the decision threshold is one of the most common strategies in these scenarios. The moving threshold technique developed in this paper is simply a greedy search of the set parameters  $w_i$ , with  $i \in \{\text{NF}, \text{F}, \text{PBL}\}$ , in an equally spaced grid  $[0, 1] \times [0, 1]$  that maximizes the chosen score expressing the classification performance. The metric adopted for the binary problem is the True Skill Score (TSS)

$$TSS = \frac{TP}{TP + FN} - \frac{FP}{FP + TN} \quad (1)$$

with TP being true-positive, FP false-positive, TN true-negative, and FN false-negative. The TSS metric is defined as the difference between the probability of detection, the first term right-hand side in (1), and the false-positive rate; it ranges between -1 and 1, and it maximizes when the probability of detecting TP is maximum, and simultaneously the ratio of FP is minimum. For the multi-classification algorithm, the score is defined as

$$MCS = 0.25 * \frac{FP_{NF}}{FP_{NF} + TN_{NF}} + 0.75 * TSS, \quad (2)$$

where  $FP_{NF}$  and  $TN_{NF}$  are the false positive and true negative, respectively, as defined considering only the "NoFreq" class. This custom score emphasizes minimizing the amount of misinformation passing between the two ML stages. For this specific task, the two performance metrics proved to be the best choice for implementing an operational tool, having as the first objective the need to minimize the amount of erroneous information, as we will largely appreciate in the next section. In this application, the latter represents the FLR frequencies estimated when it is impossible to detect resonances. In other words, the main aim was to minimize the number of "NoFreq" samples classified as "Freq" in the first ML stage; this reduces the errors propagating between the two steps. The parameters resulting from this procedure can be used to update the output probability for each class obtained from the classifier, as  $\tilde{p}_i = w_i p_i / \sum_i w_i$ . The class with the highest modified probability  $\tilde{p}_i$  will give the final classification. Other techniques for dealing with unbalanced data can be adopted, such as resampling the data set

or generating synthetic samples for the minority class (Wang et al. 2021; Kumar et al. 2022). However, these approaches modify the initial ratio between classes, which is another important feature for creating a proper operational algorithm and thus should be kept fixed as in a real case scenario, also during the training/validation stage of the algorithm. On the contrary, the moving threshold is a kind of penalization technique where particular attention is paid to minority classes, because misclassification of these samples usually does not affect the overall performance of the algorithm, even using appropriate metrics sensitive to unbalanced data sets (e.g., F1-score, Area Under the Curve, G-Mean, k-Cohen, and many others) (McHugh 2012; Cuadros-Rodríguez et al. 2016). In addition, it can be run routinely to update the model weights as the ratio between classes changes.

## 4 Results and discussion

We analyzed the performance of the classification algorithm, paying particular attention to the percentage of false positives, representing the amount of incorrect information provided by our model, since the tool must be as accurate as possible for operational purposes. As explained, we followed the same approach in choosing the proper metric for the moving threshold technique. In this section, we first evaluate the performance of the implemented classification algorithm against a binary (i.e., “Freq”/“NoFreq”) and then with a multi-class problem (i.e., “Freq”/“NoFreq”/“PBL”). Moving threshold results are presented for both applications, and performance is measured using the confusion matrix. It represents a straightforward visualization in a specific table whose cells identify the percentage of false (true) positive and (false) true negative (Stehman 1997) and allows for a direct evaluation of the amount of incorrect (correct) information provided by our algorithm. Finally, the classification technique is tested in combination with the ML algorithm implemented in Foldes et al. (2021) to determine the FLR values. The case study comprises seventeen days between the 5th and 22nd of September 2017; it includes a geomagnetic storm, quiet periods, and a couple of days where the FLR frequency was selected in correspondence with a cross-phase minimum, and so presumably the station pair was probing inside a steep plasmasphere boundary layer.

### 4.1 Binary classification

A binary classifier is the most basic classification algorithm that can be developed; moreover, in our data set, the simple division in “Freq” or “NoFreq” samples significantly reduces the class unbalance, as highlighted in Fig. 1(a)–(b). Also, in this case, however, we employ the moving threshold technique for fine-tuning the algorithm. It is worth recalling that

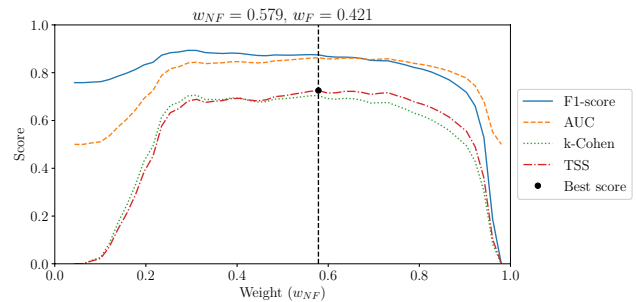


**Fig. 3** The behavior of different evaluation metrics, namely F1-score (blue solid curve), Area Under the Curve (AUC, orange dashed), k-Cohen coefficient (green dotted), and True Skill Score (TSS, red dot-dashed), as a function of the weight  $w_i$  adopted for rescaling the classification probabilities. The curves span over the weight for class 1 (“No Freq.”), and the other weight is defined as  $w_2 = 1 - w_1$ . The black vertical dashed line indicates the optimal weight obtained by looking at the TSS maximum (black dot) (color figure online)

for a perfectly balanced data set (equal number of samples per class  $N_1 = N_2$ ), the moving threshold would return equal thresholds for the two classes  $w_1 = w_2 = 0.5$ . The results for choosing the optimal threshold are represented in Fig. 3. Several metrics are shown, together with the selected one (True Skill Score, TSS, red dash-dotted curve), with sometimes completely different trends as the class weight  $w_{NF}$  changes. As expected, the weights appear inversely proportional to the percentage of samples per class; however, they are also affected by the chosen score. Indeed, as evidenced by comparing the various scores in Fig. 3 obtained with the moving threshold procedure, different metrics may result in different weights. Particularly evident is the difference for small  $w_{NF}$  between the F1-score (blue solid curve), the area under the curve (AUC, orange dashed curve), and the others. When  $w_{NF} \approx 0$ , all the samples are classified as “Freq”, and the amount of false negatives is null, while the number of true positives is maximized; for this reason, the F1-score, which is particularly sensitive to the correctly classified items, is still high even when the algorithm is biased. The AUC, on the other hand, has an initial value of  $\sim 0.5$ , indicating a random classifier. However, the AUC and the TSS give the same optimal thresholds,  $w_{NF} \approx 0.58$  and  $w_F \approx 0.42$ , and thus, both represent a suitable choice for our application. The results of the binary classification on the test set ( $N_{test} \approx 4,500$ ) are summarized in the three confusion matrices in Fig. 4. The main diagonal shows the percentage of data correctly classified per class (true negatives and true positives), while the values out-of-diagonal represent false negatives (lower left) and false positives (upper right). The latter, in particular, should be kept as low as possible in our ML pipeline to minimize the amount of wrong information spreading from the classification to the regression step (see Fig. 2). The percentage of correct samples is  $P_F \approx 77\%$

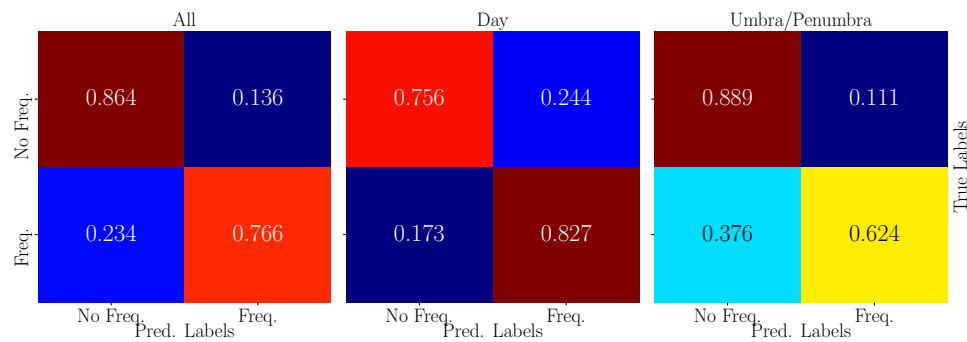


**Fig. 4** Confusion matrices (CMs) obtained from the classification of the test set. Percentages on the main diagonal represent the samples correctly classified, while the off-diagonal values are for false positives (top right) and false negatives (bottom left). The middle and

right CMs are computed *a posteriori* by looking for each sample if both the footprints are sunlit (middle) or if at least one footprint is in the dark side of the ionosphere (right)

for the “Freq” class and  $P_{NF} \approx 86\%$  for the other, while the  $\sim 14\%$  of samples, passing from the first to the second ML stage, are wrong and approximately 23% of FLR frequencies are lost during the procedure. For this reason, the algorithm could be further developed by including an additional method to handle discarded samples during the classification step; in this way, one might reduce the amount of data with a validated frequency being removed by the classifier. After the algorithm test, the samples are divided in daytime (when both footprints of the magnetic field line are sunlit) and umbra/penumbra (one or both footprints are in the dark side) to better observe how the classification errors depend on these two conditions. The results of the other two confusion matrices in Fig. 4 (center and right) highlight how changing the class ratio affects the algorithm performance; indeed, during the daytime, the number of observed frequencies is far larger than the other class, and the percentage of true positives is significantly higher  $\sim 83\%$  than the overall values  $\sim 77\%$ . The opposite happens during nighttime hours when the validated frequencies are rare and difficult to observe (Del Corpo et al. 2019; Chi et al. 2013), and thus, the percentage drastically drops to  $\sim 62\%$ . This result, in particular, suggests that more specific algorithms could be implemented in principle to work separately on diurnal and nocturnal samples to reach higher performances.

### 4.2 Multi-class classification

The same procedure has been applied to the multi-class algorithm studied in this section. Here, along with the “NoFreq” and “Freq” classes, we exploited the plasmopause position information provided by our data set to create an additional class referring to resonance frequencies measured across the plasmasphere boundary layer by TAR-BRZ, the “PBL” class (see Fig. 1). As already mentioned, in these conditions, the resonance frequencies must be searched as minima in the cross-phase spectra instead of maxima (see Del Corpo et al.

(2019) and reference therein), and therefore, some adjustments must be done to restore the typical situation. Indeed, as previously mentioned, by multiplying the cross-phase by -1 the criterion is the same as for standard resonances (i.e., detection of maxima in the cross-phase spectrum), which allows for easier automation of the regression algorithm, and consequently of the entire procedure. The complexity of adding a third class lies in the fact that we are dealing with a highly unbalanced data set, as evidenced by Fig. 1(a); indeed, the frequencies belonging to “PBL” represent a tiny percentage of the entire set. This happens, because to observe a cross-phase reversal, the location of the pair must be appropriate (ideally, both stations mapping in the plasmopause region), and the mass density variation in the plasmopause region must be quite steep [steeper than  $L^{-8}$ , (Kale et al. 2007)]. These requirements make the occurrence of cross-phase reversal quite low at all L values; in particular, Del Corpo et al. (2019) found that the maximum occurrence (with respect to the total number of FLRs detected) is about

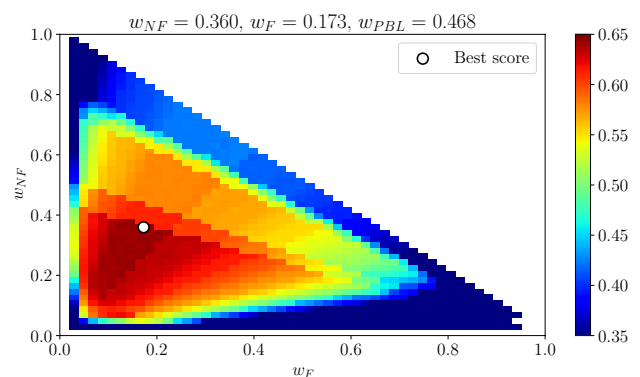


**Fig. 5** Results from the threshold optimization for the multi-classification problem. The colormap represents the score value, the evaluating metric for this task. The white circle indicates the threshold values which maximize the score (color figure online)

5% at  $L \sim 4$ , and  $\sim 1\%$  for the TAR-BRZ pair. Consequently, the moving threshold technique, whose results are shown in Fig. 5, is even more important in this case. The modified weights  $w_\alpha$  (with  $\alpha \in \{\text{NF}, \text{F}, \text{PBL}\}$ ) are inversely proportional to the percentage of samples per class, coherently to what is observed for the binary classification. There is a relatively large area (dark red) in which the optimal weights could be chosen while still maintaining high performance; however, the ratio of false negatives to false positives also varies slightly in this region. Thus, as for the binary classifier, we selected those values of  $w_i$  that minimize the number of false positives (i.e., “NoFreq” classified as “Freq”).

The results of the multi-classification approach are shown using the confusion matrices, in the same fashion as before, in Fig. 6. Interestingly, the addition of a third class seems not to affect the overall performance of the classification algorithm, which in some cases shows even higher percentage than the binary counterpart. For instance, the number of true negatives (i.e., correctly classified “NoFreq”) detected is significantly greater than  $\sim 89\%$ , resulting in a tiny percentage of false negatives (FNs), which was the main goal of our optimization. On the other hand, the number of correctly detected frequencies (true positives) slightly decreases by  $\sim 3\%$ , passing from  $\sim 77\%$  to  $\sim 74\%$ . The newly introduced class, “PBL”, shows an accuracy of  $\sim 77\%$ , whereas the remaining percentage is classified as “NoFreq”. This fact suggests that the trained algorithm tends to look for clear maxima in a specific range of frequencies where resonances occur most often at a given latitude. The analysis seems to indicate that the multi-classification approach does not significantly degrade the algorithm’s performance and can provide valuable information on the location of the plasmopause when applied to the entire EMMA network. However, the same analysis must be conducted with other stations pairs because of the different responses of the ML algorithm, as highlighted in Foldes et al. (2021). Indeed, especially at high latitudes, resonance frequencies can be very small (a few mHz), and comparable to the spectral resolution, so they are more challenging to identify. The middle and right matrices in Fig. 6 evidence the same difference between day and nighttime already observed for the binary classification.

## 5 Discussion

### 5.1 Automatic detection of FLR frequencies

In the results section, we showed the application of classification algorithms for identifying periods with observable FLR frequencies. Then, those samples can be analyzed with the ML regressor implemented in Foldes et al. (2021) for the resonance value estimation. Here, we test the two approaches combined on 17 days between the 5th and the 22nd of September 2017, allowing us to evaluate the performance of the automatic FLR detection for the TAR–BRZ stations pair ( $L = 2.9$ ). This interval of days includes a geomagnetic storm that occurred at the beginning of September 2017 and was thoroughly studied in terms of solar events and geomagnetic effects (Hajra et al. 2020). On the Sun, the occurrence of intense solar flares (Owolabi et al. 2020; Chakraborty et al. 2021), coronal mass ejections (CMEs, e.g., Werner et al. (2019)), as well as solar energetic particles (SEPs) Bruno et al. (2019); Jiggins et al. (2019) and radio bursts (Sato et al. 2019) have been extensively observed and analyzed. Subsequently, geomagnetic and geoelectric effects have been recorded in circumterrestrial space and on Earth, ranging from the plasmasphere (Obana et al. 2019; Di Mauro et al. 2021) and ionosphere (Zhang et al. 2019; Owolabi et al. 2020; Alfonsi et al. 2021) to the generation of geomagnetically induced currents (GICs, Piersanti et al. (2019)) and scintillations on the Global Navigation Satellite System (GNSS) Linty et al. (2018). Here, we report the temporal variation of the  $Kp$  index in the top panel of Fig. 7, which shows values around  $Kp \approx 8$  between the 7th and 8th of September 2017. Using a dataset with more disturbed and variable geomagnetic conditions is a more realistic and challenging test for our procedure, so we chose such a range of days. The test set proposed here is first analyzed using the multi-classification algorithm; then, all the samples classified as “Freq” or “PBL” move to the next ML stage to estimate the FLR frequency value (right block in Fig. 2). The middle panel in Fig. 7 shows the relative error

**Fig. 6** Confusion matrices (CMs) obtained from the multi-class classification of the test set. As for the previous results, the middle and right CMs are computed *a posteriori*

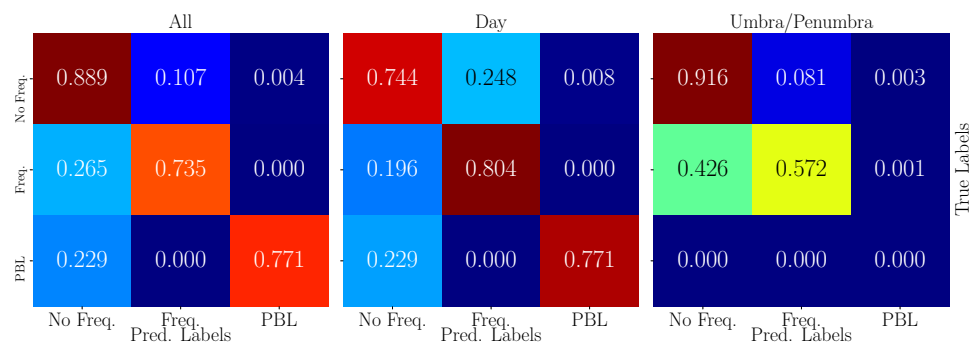
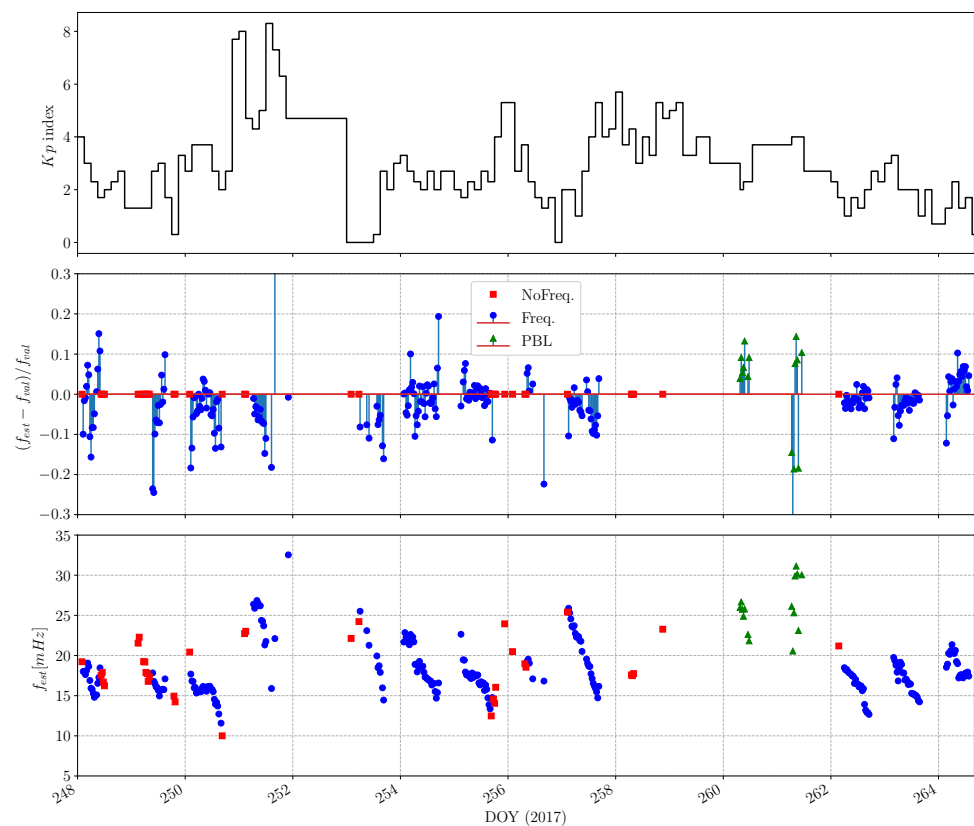


**Fig. 7** Results of combining the classification and regression ML algorithms. The first panel (top) is the daily  $Kp$  index, indicating the geomagnetic activity level. The middle panel shows the percentage error between the estimated and validated resonance frequencies, and the bottom panel highlights the estimated frequency's value (in mHz). Colors identify samples classified as "NoFreq" (red squares), "Freq" (blue circles), and "PBL" (green triangles) during the first ML stage (color figure online)



$\epsilon_r$  between the validated resonance frequency  $f_{val}$  and the frequency  $f_{est}$ , estimated using the regression algorithm in Foldes et al. (2021). The colors represent the actual class of samples, so the “NoFreq” samples (red squares) have no validated frequency from which to calculate the relative error. Errors slightly underestimate the resonance frequencies, since negative bars are usually larger than positives. However, apart for a single point, the relative error appears pretty constant, and on average around  $|\epsilon_r| \lesssim 10\%$ , for the entire interval and thus independently on the geomagnetic conditions. For the “PBL” samples (green triangles),  $\epsilon_r$  seems higher, although we do not have sufficient statistics to confirm this hypothesis in this test set. Finally, the bottom panel in Fig. 7 shows the values of the frequencies estimated by the automatic procedure, distinguished by color as before. The quasi-periodic pattern of resonances, with the frequency decreasing during the day, highlights the diurnal breathing of the plasmasphere (Park 1970). Red points, representing wrong samples passed from the classification to the regression algorithm, tend to occur either before or after long traces of recorded frequencies (blue circles), often closely following the overall behavior as shown, for instance, for DoY 250–251 and 256–257 in Fig. 7. The algorithm seems to correctly estimate higher frequency values for “PBL” points, as expected from the drop of the plasma mass density in this region.

## 5.2 Conclusion

This analysis represents a preliminary assessment of applying Machine Learning (ML) algorithms to automatically identify FLR frequencies in the inner magnetosphere using the EMMA network. Our approach, and the subsequent estimation of the plasmaspheric mass density using the Singer equation (Singer et al. 1981), represents a tool for real-time monitoring of the plasmasphere dynamics and for analyzing very long periods. The XGB classification algorithm, already adopted for regression in Foldes et al. (2021), showed reliable performance, with more than  $\sim 74\%$  of correctly detected frequencies and less than  $\sim 14\%$  of false information for both the binary and the multi-class approaches. The results generally do not depend on geomagnetic activity, as highlighted in Foldes et al. (2021). The sample analyzed here is too short to confirm the statement; in addition, at different latitudes, the geomagnetic activity might affect the results differently. The automated procedure proposed here is not primarily intended to replace semi-automated pipelines, which are a more accurate approach, because they include the knowledge of experienced users. However, we believe that ML methods may be successful for their efficiency and versatility, especially for the nowcasting and forecasting of the plasmasphere mass density and the analysis of long periods, allowing the production of significant statistics. The present results need

to be confirmed mainly using several pairs of magnetometer stations of the EMMA network and extending the data set to include more different geomagnetic conditions.

**Acknowledgements** This work is partially supported by Italian MIUR-PRIN grant 2017APKP7T\_004 on *Circumterrestrial Environment: Impact of Sun–Earth Interaction*. The authors would like to thank the Finnish Meteorological Institute (FMI), the University of Oulu (Finland), the Institute of Geophysics of the Polish Academy of Sciences (IGF-PAS), the Mining and Geological Survey of Hungary (MBFSZ), and the University of L'Aquila for contributing to EMMA. The work is also supported by the CAESAR project for the development of the ASPIS prototype of the scientific data center for Space Weather through the agreement ASI-INAF n.2020-35-HH.0 between the Italian Space Agency and the National Institute of Astrophysics. We also acknowledge the use of NASA/GSFC's Space Physics Data Facility's OMNIWeb service, and OMNI data.

**Funding** The funders had no role in the design of the study; in the collection, analyses, or interpretation of data; in the writing of the manuscript, or in the decision to publish the results.

**Data availability** Data are available at <https://doi.org/10.5281/zenodo.8321186>. The classification algorithm is available from the corresponding author, R.F., upon reasonable request.

## Declarations

**Conflict of interest** The authors declare no conflicts of interest.

## References

- Alfonsi L, Cesaroni C, Spogli L, Regi M, Paul A, Ray S, Lepidi S, Di Mauro D, Haralambous H, Oikonomou C, Shreedevi PR, Sinha AK (2021) Ionospheric disturbances over the indian sector during 8 september 2017 geomagnetic storm: Plasma structuring and propagation. *Space Weather*, 19(3):e2020SW002607. <https://doi.org/10.1029/2020SW002607>
- Allan W, Knox F (1979) A dipole field model for axisymmetric alfvén waves with finite ionosphere conductivities. *Planet Space Sci* 27(1):79–85. [https://doi.org/10.1016/0032-0633\(79\)90149-1](https://doi.org/10.1016/0032-0633(79)90149-1)
- Balasis G, Aministraglia-Giamini S, Papadimitriou C, Daglis IA, Anastasiadis A, Haagmans R (2019) A machine learning approach for automated ulf wave recognition. *J Space Weather Space Clim*. <https://doi.org/10.1051/swsc/2019010>
- Baransky L, Borovkov J, Gokhberg M, Krylov S, Troitskaya V (1985) High resolution method of direct measurement of the magnetic field lines' eigen frequencies. *Planet Space Sci* 33(12):1369–1374. [https://doi.org/10.1016/0032-0633\(85\)90112-6](https://doi.org/10.1016/0032-0633(85)90112-6)
- Bruno A, Christian ER, de Nolfo GA, Richardson IG, Ryan JM (2019) Spectral analysis of the september 2017 solar energetic particle events. *Space Weather* 17(3):419–437. <https://doi.org/10.1029/2018SW002085>
- Carpenter DL, Anderson RR (1992) An ISEE/whistler model of equatorial electron density in the magnetosphere. *J Geophys Res* 97(A2):1097–1108. <https://doi.org/10.1029/91JA01548>
- Carpenter DL, Lemaire J (2004) The plasmasphere boundary layer. *Annales Geophysicae* 22(12):4291–4298. <https://doi.org/10.5194/angeo-22-4291-2004>
- Chakraborty M, Singh A, Rao S (2021) Solar flares and geomagnetic storms of september 2017: their impacts on the tec over 75°e longitude sector. *Adv Space Res* 68(4):1825–1835. <https://doi.org/10.1016/j.asr.2021.04.012>
- Chappell CR (2015) The role of the ionosphere in providing plasma to the terrestrial magnetosphere—an historical overview. *Space Sci Rev* 192(1):5–25. <https://doi.org/10.1007/s11214-015-0168-5>
- Chen T, Guestrin C (2016) Xgboost: A scalable tree boosting system. In *Proceedings of the 22nd ACM SIGKDD International Conference on Knowledge Discovery and Data Mining*, New York, USA. <https://doi.org/10.1145/2939672.2939785>
- Chi PJ, Engebretson MJ, Moldwin MB, Russell CT, Mann IR, Hairston MR, Reno M, Goldstein J, Winkler LI, Cruz-Abeyro JL, Lee D-H, Yumoto K, Dalrymple R, Chen B, Gibson JP (2013) Sounding of the plasmasphere by Mid-continent MAGnetoseismic Chain (McMAC) magnetometers. *J Geophys Res* 118(6):3077–3086. <https://doi.org/10.1002/jgra.50274>
- Cho J, Lee D-Y, Kim J-H, Shin D-K, Kim K-C, Turner D (2015) New model fit functions of the plasmopause location determined using themis observations during the ascending phase of solar cycle 24. *J Geophys Res* 120(4):2877–2889. <https://doi.org/10.1002/2015JAG01030>
- Cuadros-Rodríguez L, Pérez-Castaño E, Ruiz-Samblás C (2016) Quality performance metrics in multivariate classification methods for qualitative analysis. *TrAC Trends in Analytical Chemistry*, 80:612–624, ISSN 0165-9936. <https://doi.org/10.1016/j.trac.2016.04.021>. URL <https://www.sciencedirect.com/science/article/pii/S016599361630084X>
- Cummings WD, O'Sullivan RJ (1969) Standing alfvén waves in the magnetosphere. *J Geophys Res* 74(3):778–793. <https://doi.org/10.1029/JA074i003p00778>
- Del Corpo A, Vellante M (2023) Plasmasphere refilling after the 1 June 2013 geomagnetic storm. *Remote Sens* 15(8):2016. <https://doi.org/10.3390/rs15082016>
- Del Corpo A, Vellante M, Heilig B, Pietropaolo E, Reda J, Lichtenberger J (2019) Observing the cold plasma in the earth's magnetosphere with the emma network. *Ann Geophys* 62(4):1. <https://doi.org/10.4401/ag-7751>
- Del Corpo A, Vellante M, Heilig B, Pietropaolo E, Reda J, Lichtenberger J (2020) An empirical model for the dayside magnetospheric plasma mass density derived from EMMA magnetometer network observations. *J Geophys Res* 125(2):2019027381. <https://doi.org/10.1029/2019JA027381>
- Del Corpo A, Zhelavskaya I, Shprits Y, Heilig B, Reda J, Pietropaolo E, Lichtenberger J (2022) Study of the average ion mass of the dayside magnetospheric plasma. *J Geophys Res* 127:10. <https://doi.org/10.1029/2022JA030605>
- Di Mauro D, Regi M, Lepidi S, Del Corpo A, Dominici G, Bagiacchi P, Benedetti G, Cafarella L (2021) Geomagnetic activity at lampedusa island: characterization and comparison with the other Italian observatories, also in response to space weather events. *Remote Sens* 13(16):3111. <https://doi.org/10.3390/rs13163111>
- Foldes R, Del Corpo A, Pietropaolo E, Vellante M (2021) Assessing machine learning techniques for identifying field line resonance frequencies from cross-phase spectra. *J Geophys Res* 126(5):e2020JA029008. <https://doi.org/10.1029/2020JA029008>
- Foldes R, Del Corpo A, Pietropaolo E, Vellante M (2023) *Field Line Resonances estimated using Machine Learning methods*. ver. 2.0.0 [Data set] Zenodo. <https://doi.org/10.5281/zenodo.8321186>
- Goldstein J, Pascuale S, Kurth WS (2019) Epoch-based model for stormtime plasmopause location. *J Geophys Res* 124(6):4462–4491. <https://doi.org/10.1029/2018JA025996>
- Hajra R, Tsurutani BT, Lakhina GS (2020) The complex space weather events of 2017 september. *Astrophys J* 899(1):3. <https://doi.org/10.3847/1538-4357/aba2c5>
- Jiggins P, Clavie C, Evans H, O'Brien TP, Witasse O, Mishev AL, Nieminen P, Daly E, Kalegaev V, Vlasova N, Borisov S, Benck S, Poivey C, Cyamukungu M, Mazur J, Heynderickx D, Sandberg I, Berger T, Usoskin IG, Paassilta M, Vainio R, Straube U, Müller D, Sánchez-Cano B, Hassler D, Praks J, Niemelä P,

- Leppinen H, Punkkinen A, Aminalragia-Giamini S, Nagatsuma T (2019) In situ data and effect correlation during september 2017 solar particle event. *Space Weather* 17(1):99–117. <https://doi.org/10.1029/2018SW001936>
- Kale ZC, Mann IR, Waters CL, Goldstein J, Menk FW, Ozeke LG (2007) Ground magnetometer observation of a cross-phase reversal at a steep plasmopause. *J Geophys Res* 112(A10):A10222. <https://doi.org/10.1029/2007JA012367>
- Kumar A, Goel S, Sinha N, Bhardwaj A (2022) A review on unbalanced data classification. In M. S. Uddin, P. K. Jamwal, and J. C. Bansal, editors, *Proceedings of International Joint Conference on Advances in Computational Intelligence*, pages 197–208, Singapore. Springer Nature Singapore
- Laurenza M, Del Moro D, Alberti T, Battiston R, Benella S, Benvvenuto F, Berrilli F, Bertello I, Bertucci B, Biasiotti L, Campi C, Carbone V, Casolino M, Cecchi Pestellini C, Chiappetta F, Coco I, Colombo S, Consolini G, D'Amicis R, De Gasperis G, De Marco R, Del Corpo A, Diego P, Di Felice V, Di Fino L, Di Geronimo C, Faldi F, Ferrente F, Feruglio C, Fiandrini E, Fiore F, Foldes R, Formato V, Francisco G, Giannattasio F, Giardino M, Giobbi P, Giovannelli L, Giusti M, Gorgi A, Heilig B, Iafra G, Ivanovski SL, Jerse G, Korsos MB, Lepreti F, Locci D, Magnafico C, Mangano V, Marcucci MF, Martucci M, Massetti S, Micela G, Milillo A, Miteva R, Molinaro M, Mugatwala R, Mura A, Napoletano G, Narici L, Neubüser C, Nisticó G, Pauluzzi M, Perfetti A, Perri S, Petralia A, Pezzopane M, Piersanti M, Pietro Paolo E, Pignalberi A, Plainaki C, Polenta G, Primavera L, Romoli G, Rossi M, Santarelli L, Santi Amantini G, Siciliano F, Sindoni G, Spadoni S, Sparvoli R, Stumpo M, Tomassetti N, Tozzi R, Vagelli V, Vasantharaju N, Vecchio A, Vellante M, Vernetto S, Vigorito C, West MJ, Zimbaro G, Zucca P, Zuccarello F, Zuccon P (2023) The CAESAR project for the asi space weather infrastructure. *Remote Sensing*, 15(2). ISSN 2072-4292. <https://doi.org/10.3390/rs15020346>
- Lichtenberger J, Clilverd MA, Heilig B, Vellante M, Manninen J, Rodger CJ, Collier AB, Jørgensen AM, Reda J, Holzworth RH et al (2013) The plasmasphere during a space weather event: first results from the PLASMON project. *J Space Weather Space Clim* 3:A23. <https://doi.org/10.1051/swsc/2013045>
- Liemohn MW (2006) Introduction to special section on “results of the national science foundation geospace environment modeling inner magnetosphere/storms assessment challenge.” *J Geophys Res* 111:A11S01. <https://doi.org/10.1029/2006JA011970>
- Linty N, Minetto A, Dovis F, Spogli L (2018) Effects of phase scintillation on the gnss positioning error during the september 2017 storm at svalbard. *Space Weather* 16(9):1317–1329. <https://doi.org/10.1029/2018SW001940>
- Liu X, Liu W, Cao JB, Fu HS, Yu J, Li X (2015) Dynamic plasmopause model based on themis measurements. *J Geophys Res* 120(12):10. <https://doi.org/10.1002/2015JA021801>
- McHugh M (2012) Interrater reliability: The kappa statistic. *Biochemia medica : časopis Hrvatskoga društva medicinskih biokemičara / HDMB*, 22:276–82. <https://doi.org/10.11613/BM.2012.031>
- Menk FW, Mann IR, Smith AJ, Waters CL, Clilverd MA, Milling DK (2004) Monitoring the plasmopause using geomagnetic field line resonances. *J Geophys Res* 109:A04216. <https://doi.org/10.1029/2003JA010097>
- Obana Y, Menk FW, Sciffer MD, Waters CL (2008) Quarter-wave modes of standing alfvén waves detected by cross-phase analysis. *J Geophys Res* 113:A8. <https://doi.org/10.1029/2007JA012917>
- Obana Y, Waters CL, Sciffer MD, Menk FW, Lysak RL, Shiokawa K, Hurst AW, Petersen T (2015) Resonance structure and mode transition of quarter-wave ulf pulsations around the dawn terminator. *J Geophys Res* 120(6):4194–4212. <https://doi.org/10.1002/2015JA021096>
- Obana Y, Maruyama N, Shinbori A, Hashimoto KK, Fedrizzi M, Nosé M, Otsuka Y, Nishitani N, Hori T, Kumamoto A, Tsuchiya F, Matsuda S, Matsuoka A, Kasahara Y, Yoshikawa A, Miyoshi Y, Shinohara I (2019) Response of the ionosphere-plasmasphere coupling to the september 2017 storm: What erodes the plasmasphere so severely? *Space Weather* 17(6):861–876
- O'Brien TP, Moldwin MB (2003) Empirical plasmopause models from magnetic indices. *Geophys Res Lett* 30(4):1152. <https://doi.org/10.1029/2002GL016007>
- Owolabi C, Lei J, Bolaji OS, Ren D, Yoshikawa A (2020) Ionospheric current variations induced by the solar flares of 6 and 10 september 2017. *Space Weather* 18(11):e2020002608. <https://doi.org/10.1029/2020SW002608>
- Ozhogin P, Tu J, Song P, Reinisch BW (2012) Field-aligned distribution of the plasmaspheric electron density: An empirical model derived from the IMAGE RPI measurements. *J Geophys Res* 117:A06225. <https://doi.org/10.1029/2011JA017330>
- Park CG (1970) (1970) Whistler observations of the interchange of ionization between the ionosphere and the protonosphere. *J Geophys Res* 75(22):4249–4260. <https://doi.org/10.1029/JA075i022p04249>
- Pezzopane M, Del Corpo A, Piersanti M, Cesaroni C, Pignalberi A, Di Matteo S, Spogli L, Vellante M, Heilig B (2019) On some features characterizing the plasmasphere-magnetosphere-ionosphere system during the geomagnetic storm of 27 May 2017. *Earth Planets Space* 71:08. <https://doi.org/10.1186/s40623-019-1056-0>
- Pierrard V, Voiculescu M (2011) The 3d model of the plasmasphere coupled to the ionosphere. *Geophys Res Lett* 38:12. <https://doi.org/10.1029/2011GL047767>
- Piersanti M, Alberti T, Bemporad A, Berrilli F, Bruno R, Capparelli V, Carbone V, Cesaroni C, Consolini G, Cristaldi A, Del Corpo A, Del Moro D, Di Matteo S, Ermolli I, Fineschi S, Giannattasio F, Giorgi F, Giovannelli L, Guglielmino SL, Laurenza M, Lepreti F, Marcucci MF, Martucci M, Mergè M, Pezzopane M, Pietro Paolo E, Romano P, Sparvoli R, Spogli L, Stangalini M, Vecchio A, Vellante M, Villante U, Zuccarello F, Heilig B, Reda J, Lichtenberger J (2017) Comprehensive Analysis of the Geoeffective Solar Event of 21 June 2015: Effects on the Magnetosphere, Plasmasphere, and Ionosphere Systems. *Solar Physics* 292(11):169. <https://doi.org/10.1007/s11207-017-1186-0>
- Piersanti M, Di Matteo S, Carter BA, Currie J, D'Angelo G (2019) Geoelectric field evaluation during the september 2017 geomagnetic storm: Maigic model. *Space Weather* 17(8):1241–1256. <https://doi.org/10.1029/2019SW002202>
- Ripoll JF, Pierrard V, Cunningham GS, Chu X, Sorathia KA, Hartley DP, Thaller SA, Merkin VG, Delzanno GL, De Pascuale S, Ukhorskiy AY (2023) Modeling of the cold electron plasma density for radiation belt physics. *Frontiers in Astronomy and Space Sciences*, 10. ISSN 2296-987X. <https://doi.org/10.3389/fspas.2023.1096595>
- Roberts WT Jr, Horwitz JL, Comfort RH, Chappell CR, Waite JH Jr, Green JL (1987) Heavy ion density enhancements in the outer plasmasphere. *J Geophys Res* 92(A12):13499–13512. <https://doi.org/10.1029/JA092iA12p13499>
- Sandel BR, Goldstein J, Gallagher DL, Spasojevic M (2003) Extreme ultraviolet imager observations of the structure and dynamics of the plasmasphere. *Space Sci Rev* 109:25–46. <https://doi.org/10.1023/B:SPAC.0000007511.47727.5b>
- Sato H, Jakowski N, Berdermann J, Jiricka K, Heßelbarth A, Banyás D, Wilken V (2019) Solar radio burst events on 6 september 2017 and its impact on gnss signal frequencies. *Space Weather* 17(6):816–826. <https://doi.org/10.1029/2019SW002198>
- Singer H, Southwood D, Walker R, Kivelson M (1981) Alfvén wave resonances in a realistic magnetospheric magnetic field geometry. *J Geophys Res* 86(A6):4589–4596. <https://doi.org/10.1029/JA086iA06p04589>

- Stehman SV (1997) Selecting and interpreting measures of thematic classification accuracy. *Remote Sens Environ* 62(1):77–89. [https://doi.org/10.1016/S0034-4257\(97\)00083-7](https://doi.org/10.1016/S0034-4257(97)00083-7)
- Stumpo M, Benella S, Laurenza M, Alberti T, Consolini G, Marcucci MF (2021) Open issues in statistical forecasting of solar proton events: a machine learning perspective. *Space Weather* 19(10):e2021002794. <https://doi.org/10.1029/2021SW002794>
- Thorne RM (2010) Radiation belt dynamics: the importance of wave-particle interactions. *Geophys Res Lett* 37:L22107. <https://doi.org/10.1029/2010GL044990>
- Vellante M, Takahashi K, Del Corpo A, Zhelavskaya I, Goldstein J, Mann I, Pietropaolo E, Reda J, Heilig B (2021) Multi-instrument characterisation of magnetospheric cold plasma dynamics in the 22 June 2015 geomagnetic storm. *J Geophys Res* 126:06. <https://doi.org/10.1029/2021JA029292>
- Wang L, Han M, Li X, Zhang N, Cheng H (2021) Review of classification methods on unbalanced data sets. *IEEE Access* 9:64606–64628. <https://doi.org/10.1109/ACCESS.2021.3074243>
- Waters CL, Menk FW, Fraser BJ (1991) The resonance structure of low latitude Pc3 geomagnetic pulsations. *Geophys Res Lett* 18(12):2293–2296. <https://doi.org/10.1029/91GL02550>
- Werner ALE, Yordanova E, Dimmock AP, Temmer M (2019) Modeling the multiple cme interaction event on 6–9 september 2017 with wsa-enlil+cone. *Space Weather* 17(2):357–369. <https://doi.org/10.1029/2018SW001993>
- Zhang S-R, Erickson PJ, Coster AJ, Rideout W, Vierinen J, Jonah O, Goncharenko LP (2019) Subauroral and polar traveling ionospheric disturbances during the 7–9 september 2017 storms. *Space Weather* 17(12):1748–1764. <https://doi.org/10.1029/2019SW002325>

**Publisher's Note** Springer Nature remains neutral with regard to jurisdictional claims in published maps and institutional affiliations.

Springer Nature or its licensor (e.g. a society or other partner) holds exclusive rights to this article under a publishing agreement with the author(s) or other rightsholder(s); author self-archiving of the accepted manuscript version of this article is solely governed by the terms of such publishing agreement and applicable law.